Numerical analysis of the dynamic behavior of rotor shafts in permanent magnet synchronous machines

Thomas Poupon, Nicolas Abdelnour, Arthur Givois, Vincent Lanfranchi, Jean-Daniel Chazot, Tahar Hamiti, Patrice Caule

Numerical analysis of the dynamic behavior of rotor shafts in permanent magnet synchronous machines

Thomas POUPON[1,3], Nicolas ABDELNOUR[1,3], Arthur GIVOIS[1], Vincent LANFRANCHI[1], Jean-Daniel CHAZOT[1], Tahar HAMITI[2], and Patrice CAULE[3]

[1]Roberval - Université de Technologie de Compiègne, Roberval (Mechanics, energy and electricity), Centre de recherche Royallieu - CS 60319 - 60203 Compiègne cedex, France
[2]Emotors, 212, Bd Pelletier - 78 955 Carrieres-Sous-Poissy, France
[3]Safran Ventilation Systems, Blagnac, FRANCE

Abstract

In order to design permanent magnets synchronous machines as quiet as possible, we propose a predictive magneto-mechanical vibration model. This model allows for describing the dynamics of the system under operating conditions by including a strong magneto-mechanical coupling between the electromagnetic forces and the dynamics of the motor shaft. The Maxwell pressures are calculated analytically using the subdomain method, while the rotor dynamics are based on a 1D beam model. The coupling between these two physical phenomena is solved using time integration. This numerical study aims first at highlighting the strong coupling regimes and their influence on the harmonic content of the displacement. The second objective is concerned with the study of the influence of static eccentricity on the spectral content of the dynamic response.

1 Introduction

The dynamic behavior of the rotor plays a key role in the overall response of electric machines. This requires complex modeling that takes into account two distinct physical phenomena, namely electromagnetism and mechanics. The question of the coupling between these two fields should be addressed carefully. In this study, a mechanical model is developed to describe the vibratory behavior of the rotor. The rotor is subjected to magnetic forces which depend on mechanical displacement. In this framework, a weak coupling is often made (no magneto-mechanical interaction). The objective of this article is to show numerically the influence of strong coupling.

1.1 Magnetic model

The magnetic forces acting on the rotor come from different origins: magnetostrictive deformations (internal forces in the materials) and Maxwell forces (forces at the interfaces of the materials). Several studies have shown that the magnetostrictive force is negligible in the context of electrical machines (see [1]). Thus, in this work, only the Maxwell pressures are considered.

In the case of magnetic misalignment between the rotor and the stator, a residual force acting on the rotor, without generating torque. This force, called UMP (Unbalanced Magnetic Pull), is source of vibrations. It depends in particular on the position of the rotor relative to the stator. The objective of the magnetic model is to model this force accurately.

This force can be calculated from Maxwell's pressures, which depend on magnetic fields. Several methods can be used to determine these pressures, such as the Lehmann graphical method [2], the conformal transform method [3], the permeance function and magnetomotive force method [4], the method of the electrical equivalent circuit with a reluctance network [5], or the analytical method of sub-domains [6]. Among these methods, the subdomain analytical method offers a good compromise between computation time, complexity, and accuracy, making it an appropriate choice for our magnetic model.

1.2 Mechanical model

The study of a rotating shaft is not a recent subject in mechanics. The first studies were carried out by De Laval, and later by Jeffcott [7]. They introduced a simplified shaft model, represented by localized mass and inertia, subjected to elastic forces that model shaft bending or bearing effects. These studies helped highlight the gyroscopic effect. This effect results in a separation of eigenmodes into two rotating eigenmodes.

Gyroscopic effects were analyzed in the work of Gmür [8] and Genta [9], where finite element and continuous models are used, assuming 1D Timoshenko beams. A comparison of both modellings will be made in this paper.

1.3 Magneto-mechanical coupling

The simplest models assume a weak coupling between the mechanical model and the magnetic model. The initial approximations involve expressing this coupling at a fixed rotor position [10]. This approximation assumes that the shaft deformation is negligible compared to the magnetic displacement. This concept is further developed by modeling the magnetic force with a negative stiffness (see Merrill [11], Han and Palazzolo [12], Rosenberg [13]). In contrast, recent studies simulate the strongly coupled mechanical response using a complete magnetic model (see [14] and [5]). This article aims to investigate the impact of strong coupling compared to weak coupling on a highly simplified mechanical structure.

2 Theoretical part

The main objective of this part is to study the influence of the magnetic force on the mechanical behavior of the rotor. For a better understanding, a complete magnetic model is utilized while the mechanical model is simplified.

The electrical machine under study is a permanent magnet synchronous machine. The magnets are positioned on the rotor surface, which has 3 pairs of magnetic poles and 36 open slots in the stator. The shaft is cylindrical, made of steel, and has a length of $L = 0.5m$. Mechanical and magnetic characteristics of the study case are presented in Table 1.

$L(m)$	$R(mm)$	$\rho(kg/m^3)$	$E(GPa)$	ν	I_p	k'	G	A
$0,5$	30	7850	210	$0,29$	$\pi R^4/2$	$5/6$	$E/2/(1+\nu)$	πR^2

Number of pole pairs	Number of slots	Outer rotor radius (mm)	Inner stator radius (mm)	Magnetic stacks size
3	36	$31,05$	$32,5$	$L/3$

Table 1: Mechanical and magnetic data of the machine

2.1 Mechanical model

The rotor shaft is modeled using a 1D Timoshenko beam model that takes gyroscopic effects into account. We assume a constant rotation speed of the shaft, denoted as Ω. The magnetic forces are applied to the beam's center over a length of $\Delta L = 0.02m$. The expression for the linear force is presented in the next subsection.

We denote $(\mathbf{x}, \mathbf{y}, \mathbf{z})$ as the fixed reference frame relative to the stator, and $(\mathbf{x}_2, \mathbf{y}_2, \mathbf{z}_2)$ as the rotating frame fixed on the rotor. An intermediate frame $(\mathbf{x}_1, \mathbf{y}_1, \mathbf{z}_1)$ is used to define the two rotations between the fixed and the rotating frame (see Figure 1).

We define u_x and u_y as the displacements along the $\mathbf{x}$ and $\mathbf{y}$ axis respectively. The angles Φ and Ψ represent the degrees of freedom associated with rotations around the $\mathbf{x}$ and $\mathbf{y}_1$ axes, respectively (see Figure 1a and 1b).

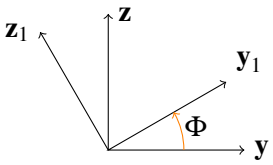

(a) Rotation of the frame $(\mathbf{x},\mathbf{y},\mathbf{z})$ around $\mathbf{x}$ axis by an angle Φ

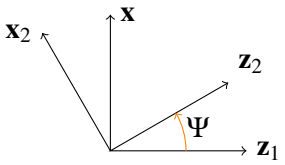

(b) Rotation of the frame $(\mathbf{x}_1,\mathbf{y}_1,\mathbf{z}_1)$ around $\mathbf{y}_1$ axis by an angle Ψ. The frame $(\mathbf{x}_2,\mathbf{y}_2,\mathbf{z}_2)$ is associated with the deformed rotor

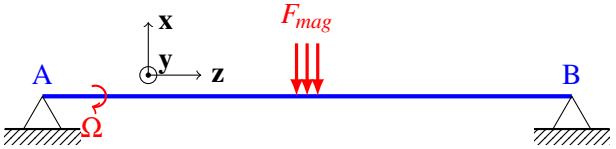

(c) 1D Timoshenko beam of length 50 cm supported at ends A and B, with a constant rotational speed of Ω, and magnetic forces applied to the center of the beam over a length of 2 cm.

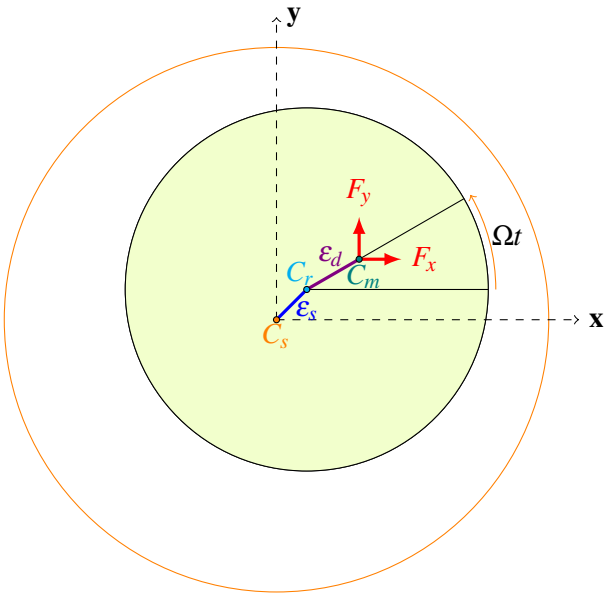

(d) Sectional view, representing the rotor in green and the stator in orange. C_s the magnetic axis of the stator, C_r the axis of rotation of the shaft, and C_m the magnetic axis of the rotor. The values ε_s and ε_d the static and dynamic eccentricities, respectively, representing the distances between the C_s and C_r axes, as well as the C_r and C_m axes. Ω constant speed of the rotor around C_r. F_x and F_y the projected magnetic resultants.

Figure 1: Diagram illustrating the rotations of the reference frame in (a) and (b), the modeled beam model in (c), and the cross-sectional diagram of the electrical machine in (d)

Let us recall the expressions for a continuous Timoshenko beam subjected to gyroscopic effects (cf. [15]):

$$\begin{cases} \rho A \frac{d^2 u_x}{dt^2} = GAk' \left(\frac{\partial^2 u_x}{\partial z^2} - \frac{\partial \Psi}{\partial z} \right) \\ \rho A \frac{d^2 u_y}{dt^2} = GAk' \left(\frac{\partial^2 u_y}{\partial z^2} + \frac{\partial \Phi}{\partial z} \right) \\ \rho I_p \frac{d^2 \Phi}{dt^2} + 2\rho I_p \Omega \frac{d\Psi}{dt} = -GAk' \left(\frac{\partial u_y}{\partial z} + \Phi \right) + EI_p \frac{\partial^2 \Phi}{\partial z^2} \\ \rho I_p \frac{d^2 \Psi}{dt^2} + 2\rho I_p \Omega \frac{d\Phi}{dt} = -GAk' \left(\frac{\partial u_x}{\partial z} + \Psi \right) + EI_p \frac{\partial^2 \Psi}{\partial z^2} \end{cases} \tag{1}$$

with A representing the cross-sectional area, ρ the density, E the Young's modulus, G the shear modulus, k' the Timoshenko shear coefficient, and I_p the polar moment of inertia about the axis of rotation. We observe the following effects: shearing effect (terms involving GAk'), rotational inertia of the section (terms involving ρI_p), and gyroscopic effects dependent on the rotation speed (terms involving $2\rho I_p \Omega$).

In the following two models are used to get the equations of motion : a finite element model, and an analytical model. The modes are then obtained from the boundary conditions. Then, two mehtods are used to solve these equations in time from initial conditions : either with a time integration scheme, or with a direct approach in the frequency domain.

2.2 Magnetic model

In this article, the magnetic fields are calculated in a cross-sectional plane of the shaft using the subdomain method. This method involves dividing the machine into different "subdomains" where the magnetic induction are analytically calculated.

Let **B** be the magnetic field. Neglecting edge effects and assuming an infinitely long cross-sectional plane, we can define the magnetic potential A_z as follows:

$$\begin{cases} B_r = \frac{1}{r}\frac{\partial A_z}{\partial \alpha} \\ B_\alpha = -\frac{\partial A_z}{\partial r} \end{cases} \tag{2}$$

Using Maxwell's equations, we obtain the following differential equation (in polar coordinates):

$$\frac{\partial^2 A_z}{\partial r^2} + \frac{1}{r}\frac{\partial A_z}{\partial r} + \frac{1}{r^2}\frac{\partial^2 A_z}{\partial \alpha^2} = 0 \tag{3}$$

We can analytically obtain the general solution of the differential equation in each subdomain:

$$A_z = \sum_{v=1}^{\infty} (Cr^v + Dr^{-v})(A\cos(v\alpha) + B\sin(v\alpha)) \tag{4}$$

The motor is divided into three regions (see Figure 2): the magnets, the air gap, and the slots. The continuity conditions between these domains couple the previous equations. By adding the source terms induced by magnetization and stator currents (perfect three-phase currents of 12A), and projecting these terms onto each previous solution, the particular solution is obtained.

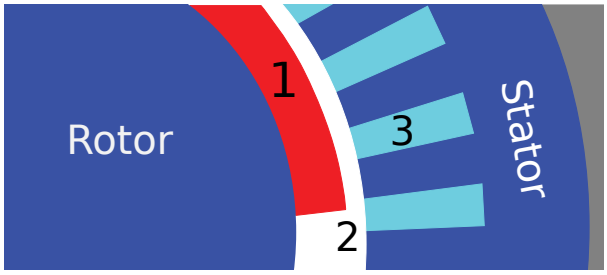

Figure 2: Diagram of the different subdomains: magnet in 1, air gap in 2, and slots in 3

Once the magnetic potential is expressed in each subdomain, the radial field B_r and tangential field B_t is written using equation (2).

The Maxwell surface pressures are then obtain using the following expression:

$$P_r = \frac{B_r^2 - B_t^2}{2\mu_0} \text{ et } P_t = \frac{B_r B_t}{\mu_0} \tag{5}$$

By integrating these pressures around the rotor, the magnetic forces is deduce, both in terms of resultant force and moment, acting on the rotor. Assuming a constant velocity, the angular description of the forces can be replaced with a time desciption. The force is finally written as follows:

$$\mathbf{f}_{mag} = \begin{pmatrix} f_x(x,y,t) \\ f_y(x,y,t) \end{pmatrix} \tag{6}$$

with (x,y) the position of the rotor magnetic center C_m. These coodinates write:

$$\begin{pmatrix} x \\ y \end{pmatrix} = \varepsilon_s \frac{\begin{pmatrix} x_0 \\ y_0 \end{pmatrix}}{\sqrt{x_0^2 + y_0^2}} + \varepsilon_d \begin{pmatrix} \cos(\Omega t) \\ \sin(\Omega t) \end{pmatrix} + \begin{pmatrix} u_x \\ u_y \end{pmatrix} \tag{7}$$

where (x_0, y_0) denote the coordinates of the center of rotation C_r, (u_x, u_y) the displacement induced by the deformation of the shaft, $\varepsilon_s = \sqrt{x_0^2 + y_0^2}$, static eccentricity correspond to the distance between the magnetic center of the stator C_s and the center of rotation C_r, and ε_d dynamic eccentricity correspods to the distance between the center of rotation C_r and the magnetic center of the rotor C_m.

A Taylor expansion around the center of rotation (x_0, y_0), leads to:

$$\mathbf{f}_{mag}(x,y,t) = \mathbf{f}_0(x_0,y_0,t) + \mathbf{K}_{mag}(t) \begin{pmatrix} u_x + \varepsilon_d \cos(\Omega t) \\ u_y + \varepsilon_d \sin(\Omega t) \end{pmatrix} + HOT(x,y,t) \tag{8}$$

with $\mathbf{f}_0$ and $\mathbf{K}_{mag}$ the zero order term and the magnetic stiffness link to the first order term in the taylor expansion and HOT Higher Order Term of the taylor expansion with respect to the displacement. When performing simulations with weak coupling, only the first-order term $\mathbf{f}_0$ is considered. Section 4 specifically addresses the contribution of these higher order terms.

Figure 3a shows the magnetic force component $\mathbf{f}_0$ during one revolution of the shaft with a static eccentricity of 10% of the air gap along the **x** axis. We observe a higher average component for the force F_x, which is consistent with the imposed direction of eccentricity.

A discrete Fourier transform is computed in Figure 3b. It highlights a high amplitude for the 6th order harmonics, which is consistent with the number of poles, as well as the 36th order harmonic which comes from the number of slots.

The magnetic model has already been confronted with finite element methods and validated (see [16]). The displacement response of the rotor is studied in the following part.

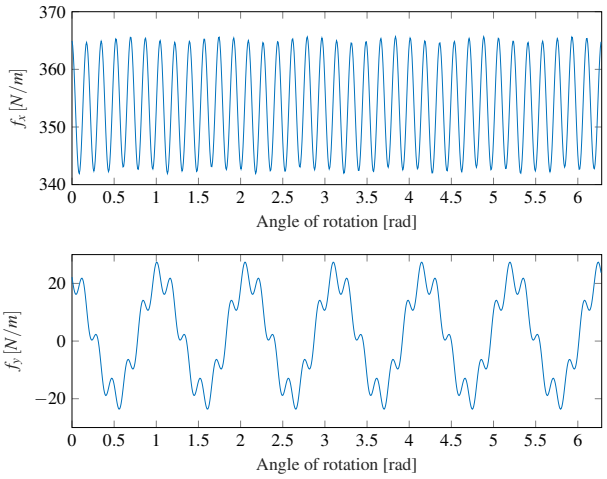

(a) Linear magnetic forces $f_x(x_0, y_0)$ and $f_y(x_0, y_0)$ with a static eccentricity ε_s of 10% of the air gap along the **x** axis as a function of the rotation angle

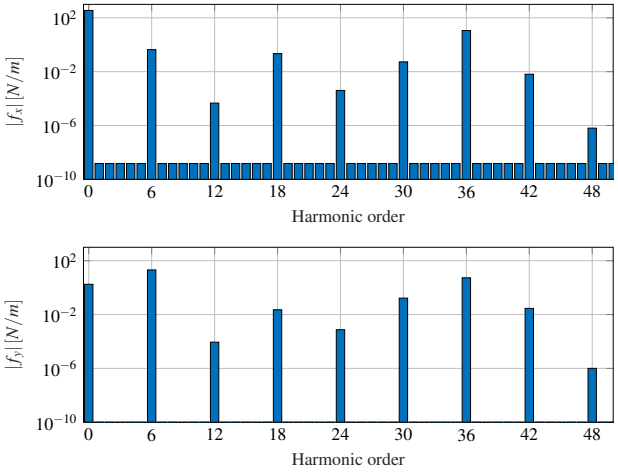

(b) Amplitude spectrum of the linear forces $f_x(x_0, y_0)$ and $f_y(x_0, y_0)$, forces generated by a machine with 3 pairs of poles and 36 slots

Figure 3: Linear magnetic forces in (a) and spectrum of these forces in (b) with 10% eccentricity along the **x** axis

3 Comparison of simulations with static eccentricity in weak coupling

To solve the couple differential equation system, two types of analysis are performed. We solve the equation in the time domain and the frequency domain.

In this paragraph, we compute our simulations in weak coupling, considering only $\mathbf{f}_0(x_0, y_0, t)$, with a modal damping of 1% and a static exccentricity of 10% along **x** axis.

3.1 Comparison of the Semi-Analytical and Finite Element Models

To study the coherence of the two models, maximum displacement of the shaft compare as a function of the assumed constant operating speed. The problem is solved algebraically, based on mode expansion.

In Figure 4a, the maximum displacement over one cycle is shown for both the finite element (FE) and semi-analytical models. The deformation peaks occur at the same frequencies. The response is slightly higher away from the peaks. This difference is due to the static influence of higher truncated modes (40 modes considered) for the analytical model, and potential numerical errors introduced by the FE method (100 elements). In Figure 4b, the harmonic content of the time response at 2000 rpm from both models : the result exhibit similar harmonic content. Therefore, we conclude that models are equivalent and provide the same information.

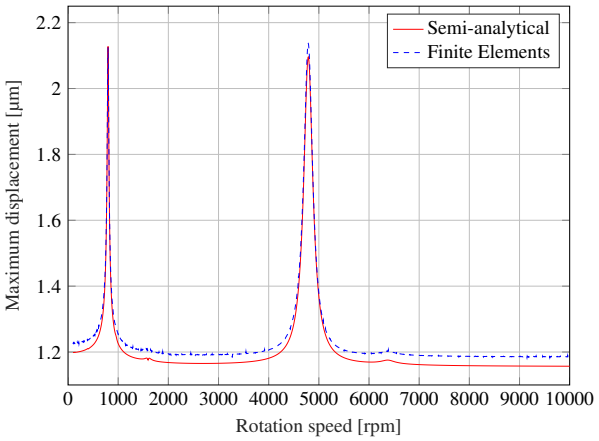

(a) Maximum displacement during one cycle on the shaft, solved by mode superposition in weak coupling using the finite element model (100 nodes) and the semi-analytical model (40 modes)

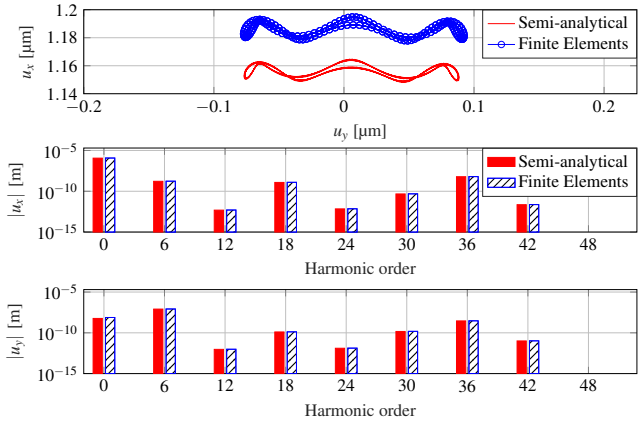

(b) Displacement of the center of the shaft over time at 2000 rpm, and Fourier transformation of u_x and u_y using the semi-analytical and finite element models

Figure 4: Comparison of analytical and finite element models in terms of maximum displacement (a) and harmonic content (b)

From a physical point of view, two resonance peaks are observed, one at 900 rpm and one at 4790 rpm. To understand their origin, a Campbell diagram is used. In Figure 5, the natural frequencies are represented in blue and red as a function of rotational speed. Under the gyroscopic effect, the frequencies of direct modes in red and indirect modes in blue separate, increasing or decreasing, respectively, depending on the rotational speed. The different harmonics present in the magnetic excitation force are plotted as dashed lines. The intersection of these harmonics with the previous frequencies indicates critical speed where a resonance. We therefore deduce than the peak of displacement at 900 rpm is excited by the 36th harmonic, while the peak at 4790 rpm is excited by the 6th harmonic.

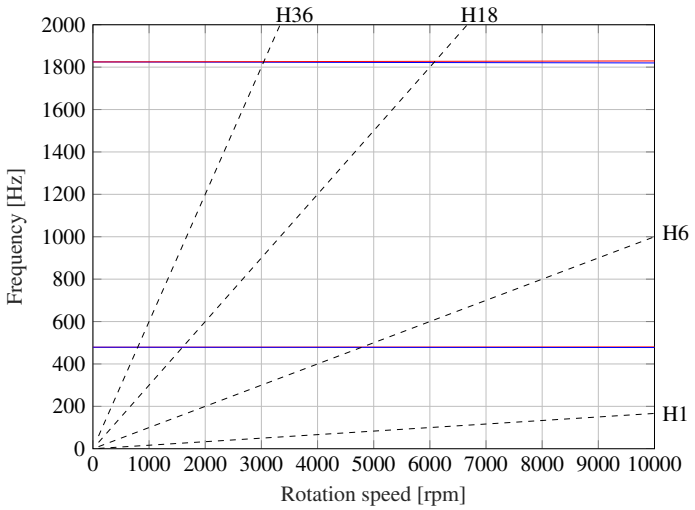

Figure 5: Campbell diagram, direct modes in red and indirect modes in blue, of a rotating Timoshenko beam (see Table 1), with the main orders of magnetic excitation 1, 6, 18, and 36 (see Fig 4b)

3.2 Comparison of the a time integration scheme with a direct approach in frequency

In this section, we perform simulations using the semi-analytical model and compare two methods for solving the time differential equations. The first method involves transforming the equations into the frequency domain and solving the problem through modal superposition. The second method involves directly solving the problem in the time domain using the ode15s integration scheme.

In Figure 6, we observe that in the case of weak coupling, both computation methods lead to similar results. However, the use of the ode15s function result in a slight decrease in the amplitude of resonance peaks (reduction of the amplitude of the resonance peak at 4785 Hz for the 6th harmonic by 2.24%). We also encounter some convergence issues with residuals at speeds below 850 rpm, due to a convergence error. Thus, we validate the ode15s time integration scheme compared to the solution based on modal expansion.

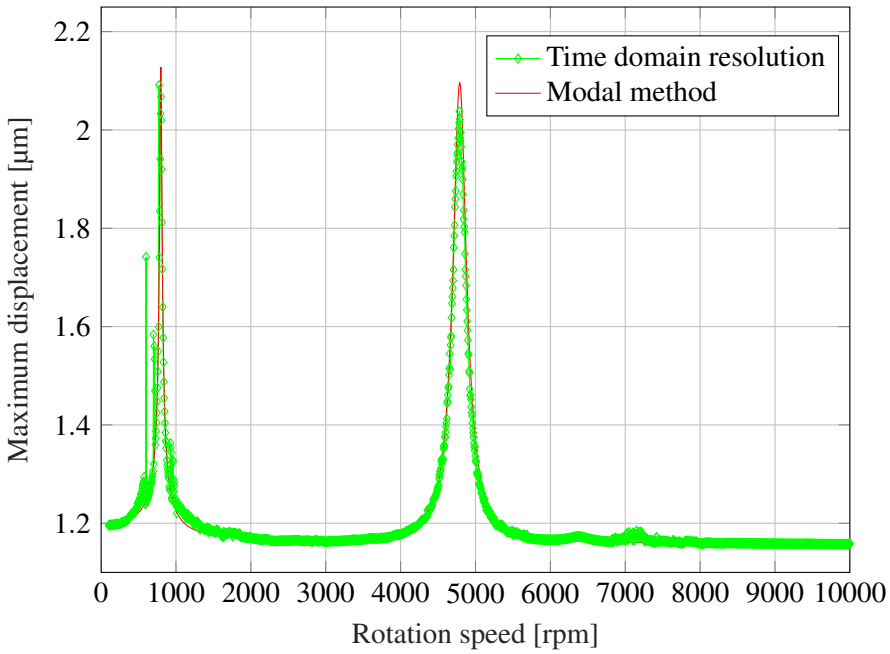

Figure 6: Spectrum of max displacements during one cycle on the shaft, resolved using modal method and the ode15s time integration function (Matlab) in weak coupling with the semi-analytical model

Now that the models and the methods conform well to each other, the semi-analytical model with the ode15s time integration method only are used in the next part.

4 Influence of strong coupling with static eccentricity

With 10% of eccentricity along the **x** axis, this time we consider the entire force $\mathbf{f}_{mag}(x,y,t)$ instead of just the zeroth-order term $\mathbf{f}_0(t)$. In Figure 7, we plot the maximum displacement response as a function of rotation speed for weak and strong coupling. We observe a shift of the maximum response peak towards lower frequencies. For example, the peak located at 4790 Hz in weak coupling is now at 4770 Hz in the case of strong coupling. This is due to the negative magnetic stiffness. The maximum displacement is also slightly higher in the case of strong coupling, but it remains of the same order of magnitude.

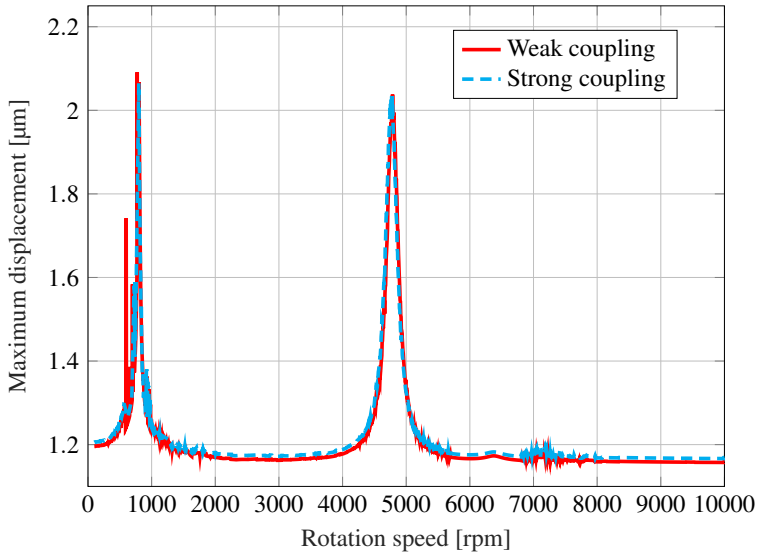

Figure 7: Maximum deformation during one cycle on the shaft, comparison between strong coupling and truncation to the zero order of the magnetic (weak coupling) force

In Figures 8a and 8b, we compare the harmonic content of displacements in the case of weak and strong coupling at 2000 rpm (off-resonance) and 4770 rpm (resonance of the 6th harmonic). At 2000 rpm, we observe a similar harmonic content, except for the 12th harmonic which shows a much larger response (130 times larger). In Figure 8b at 4770 rpm, we observe even more significant differences for the 12th harmonic (250 times larger), as well as the appearance of the 48th harmonic.

In both cases, the vibrational response is modified. The change in the harmonic response becomes more noticeable as the displacement increases.

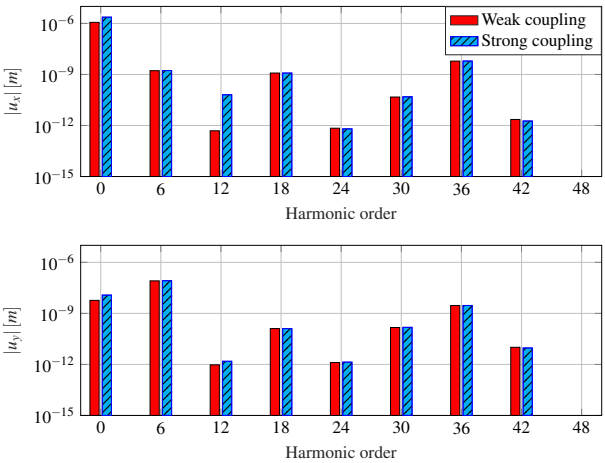

(a) Harmonic content of displacements u_x and u_y at 2000 rpm

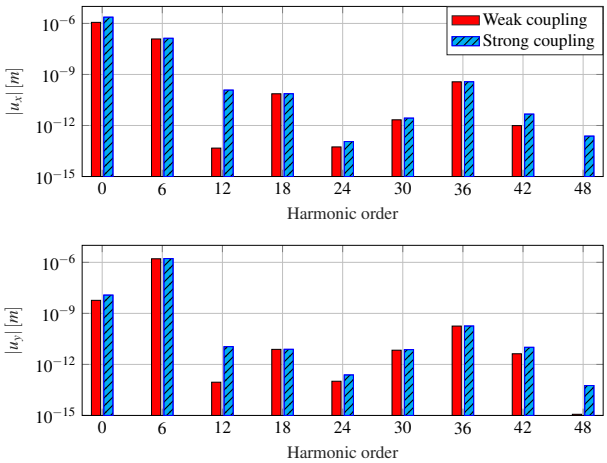

(b) Harmonic content of displacements u_x and u_y at 4770 rpm

Figure 8: Harmonic content of displacements at 2000 rpm and at 4770 rpm in weak coupling (in red) and in strong coupling (in blue)

5 Conclusion

The initial static eccentricity simulations first ensure the numerical convergence of the models (semi-analytical and finite element) as well as the simulation methods (time integration and mode superposition). By using the Campbell diagram and analyzing the harmonic content of the injected force, we were able to conclude that static eccentricity induces resonances in the beam displacement, mainly caused by the 36th and 6th harmonics of the magnetic force. The other lower amplitude harmonics do not have a significant effect on the maximum displacement amplitude. However, they do influence the overall harmonic content of the displacement.

The simulations under strong coupling revealed a slight shift in resonance frequencies and spectral differences in the response compared to weak coupling. This phenomenon is more pronounced when the maximum displacement is significant, especially in the presence of resonance of the 36th and 6th harmonics. However, outside of resonance situations, weak coupling remains valuable and provides a consistent overall approximation, with the exception of a few harmonics, such as the 12th harmonic, which sometimes reaches levels of similar magnitude as the main ones.

These displacement harmonics may not play a major role in the rotor dynamics, but could induce a higher vibratory response of the stator. Projecting these efforts onto the stator modes, along with a thorough study of the spatial orders of the P_r and P_t fields, would allow to assess the importance of these harmonics and subsequently compute acoustic radiation.

References

[1] Garvey, S. Magnetostrictive excitation of vibration in machines - a modal approach. *9th International Conference On Electrical Machines And Drives*. (1999), https://doi.org/10.1049/cp:19991012

[2] Lehmann, T. (1909) *Méthode graphique pour déterminer le trajet des lignes de force dans l'air. Revue d'Électricité : La Lumière Électrique* 43-45, 103-110 & 137-142 & 163-168.

[3] Alam, F. & Abbaszadeh, K. Magnetic Field Analysis in Eccentric Surface-Mounted Permanent-Magnet Motors Using an Improved Conformal Mapping Method. *IEEE Transactions On Energy Conversion*. **31**, 333-344 (2016,3), https://doi.org/10.1109/tec.2015.2479562

[4] Serrano-Iribarnegaray, L., Cruz-Romero, P. & Gomez-Exposito, A. CRITICAL REVIEW OF THE MODIFIED WINDING FUNCTION THEORY. *Progress In Electromagnetics Research*. **133** pp. 515-534 (2013), https://doi.org/10.2528/pier12091301

[5] Li, X., Bourdon, A., Rémond, D., Kœchlin, S. & Prieto, D. Angular-based modeling of unbalanced magnetic pull for analyzing the dynamical behavior of a 3-phase induction motor. *Journal Of Sound And Vibration*. **494** pp. 115884 (2021,3) https://www.sciencedirect.com/science/article/abs/pii/S0022460X20307215

[6] Doherty, R. & Nickle, C. Synchronous machines I-an extension of blondel's two-reaction theory. *Transactions Of The American Institute Of Electrical Engineers*. **XLV** pp. 912-947 (1926,1), https://doi.org/10.1109/t-aiee.1926.5061289

[7] Jeffcott, H. XXVII. The lateral vibration of loaded shafts in the neighbourhood of a whirling speed — The effect of want of balance. *The London, Edinburgh, And Dublin Philosophical Magazine And Journal Of Science*. **37**, 304-314 (1919,3), https://www.tandfonline.com/doi/abs/10.1080/14786440308635889

[8] Gmür, T. Dynamique des structures: Analyse modale numérique. (PPUR,2008,1), https://www.epflpress.org/produit/135/9782880748135/dynamique-des-structures

[9] Genta, G. Dynamics of Rotating Systems. (Springer London, Limited,2005), https://link.springer.com/book/10.1007/0-387-28687-X

[10] Galfarsoro, U., McCloskey, A., Zarate, S., Hernandez, X. & Almandoz, G. Influence of Manufacturing Tolerances and Eccentricities on the Unbalanced Magnetic Pull in Permanent Magnet Synchronous Motors. *IEEE Transactions On Industry Applications*. **58**, 3497-3510 (2022,5), https://doi.org/10.1109/tia.2022.3156075

[11] Merrill, E. Dynamics of AC electrical machines. *IEEE Transactions On Industry Applications*. **30**, 277-285 (1994), https://ieeexplore.ieee.org/document/287533

[12] Han, X. & Palazzolo, A. Unstable force analysis for induction motor eccentricity. *Journal Of Sound And Vibration*. **370** pp. 230-258 (2016,5), https://www.sciencedirect.com/science/article/pii/S0022460X16000948

[13] Rosenberg, E. Magnetic Pull in Electric Machines. *Transactions Of The American Institute Of Electrical Engineers*. **XXXVII**, 1425-1469 (1918,7), https://ieeexplore.ieee.org/document/4765578

[14] Abdelnour, N., Caule, P., Lanfranchi, V. & Chazot, J. Contribution to the electro-magneto-mechanic strong coupling in the study of vibration of eletric motors of aeronautic ventilation systems. (e-Forum Acusticum 2020,2020), https://hal.archives-ouvertes.fr/FA2020/hal-03235450

[15] Raffa, F. & Vatta, F. The Dynamic Stiffness Method for Linear Rotor-Bearing Systems. *Journal Of Vibration And Acoustics*. **118**, 332-339 (1996,7), https://asmedigitalcollection.asme.org/vibrationacoustics/article-abstract/118/3/332/422156/The-Dynamic-Stiffness-Method-for-Linear-Rotor

[16] Abdelnour, N. Contribution à l'étude des couplages électro-magnéto-mécaniques pour l'acoustique des machines électriques d'un système de ventilation aéronautique. (Université de Technologie de Compiègne,2021,9), https://theses.hal.science/tel-03973835